

Journal of
Applied Remote Sensing

RemoteSensing.SPIEDigitalLibrary.org

Change detection from synthetic aperture radar images based on neighborhood-based ratio and extreme learning machine

Feng Gao
Junyu Dong
Bo Li
Qizhi Xu
Cui Xie

SPIE.

Feng Gao, Junyu Dong, Bo Li, Qizhi Xu, Cui Xie, "Change detection from synthetic aperture radar images based on neighborhood-based ratio and extreme learning machine," *J. Appl. Remote Sens.* **10**(4), 046019 (2016), doi: 10.1117/1.JRS.10.046019.

Change detection from synthetic aperture radar images based on neighborhood-based ratio and extreme learning machine

Feng Gao,^a Junyu Dong,^{a,*} Bo Li,^b Qizhi Xu,^b and Cui Xie^a

^aOcean University of China, Department of Computer Science and Technology,
238 Songling Road, Qingdao 266100, China

^bBeihang University, School of Computer Science and Engineering,
Beijing Key Laboratory of Digital Media, 37 Xueyuan Road, Beijing 100191, China

Abstract. Change detection is of high practical value to hazard assessment, crop growth monitoring, and urban sprawl detection. A synthetic aperture radar (SAR) image is the ideal information source for performing change detection since it is independent of atmospheric and sunlight conditions. Existing SAR image change detection methods usually generate a difference image (DI) first and use clustering methods to classify the pixels of DI into changed class and unchanged class. Some useful information may get lost in the DI generation process. This paper proposed an SAR image change detection method based on neighborhood-based ratio (NR) and extreme learning machine (ELM). NR operator is utilized for obtaining some interested pixels that have high probability of being changed or unchanged. Then, image patches centered at these pixels are generated, and ELM is employed to train a model by using these patches. Finally, pixels in both original SAR images are classified by the pretrained ELM model. The preclassification result and the ELM classification result are combined to form the final change map. The experimental results obtained on three real SAR image datasets and one simulated dataset show that the proposed method is robust to speckle noise and is effective to detect change information among multitemporal SAR images. © 2016 Society of Photo-Optical Instrumentation Engineers (SPIE) [DOI: 10.1117/1.JRS.10.046019]

Keywords: synthetic aperture radar; change detection; neighborhood-based ratio; hierarchical fuzzy c-means clustering; extreme learning machine.

Paper 16583 received Aug. 3, 2016; accepted for publication Nov. 11, 2016; published online Dec. 1, 2016.

1 Introduction

Change detection is a process that analyzes two remote sensing images captured over the same geographical area at different times to identify significant land cover changes.¹ It is of high practical value to a large number of applications, such as hazard assessment of earthquake areas,² crop growth monitoring,³ urban sprawl detection,^{4,5} and snow cover monitoring.⁶ Therefore, change detection has drawn increasing attention in remote sensing communities. In the 2012 and 2015 data fusion contest organized by the IEEE Data Fusion Technical Committee,⁷ many techniques have been studied for change detection by using multimodal remote sensing data, such as optical,^{8,9} LiDAR,¹⁰ hyperspectral,¹¹ and synthetic aperture radar (SAR) data.¹²

Among the aforementioned multimodal data, SAR is the ideal information source for performing change detection, since SAR sensors are independent of atmospheric and sunlight conditions.¹³ Therefore, SAR images can be acquired under all weather and all day, which can make up for the shortage of optical and LiDAR remote sensing. Especially when heavy rain causes severe flooding, SAR images are highly effective for detecting land cover change, since optical data are rarely available.¹² In addition, with the development of earth observation

*Address all correspondence to: Junyu Dong, E-mail dongjunyu@ouc.edu.cn

programs, more and more SAR sensors have been developed to collect hundreds of images for the same area on the earth's surface at shorter intervals.¹⁴ Hence, change detection by using SAR images becomes more and more important. However, SAR image change detection exhibits more difficulties than optical ones due to the presence of the multiplicative speckle noise.¹ It is essential to develop a robust SAR image change detection technique against the speckle noise.

In the literature, many techniques have been recently developed for SAR image change detection. Generally, these techniques are often comprised of three steps:¹⁵ (1) coregistration and geometric corrections, (2) difference image (DI) generation, and (3) unsupervised or supervised classification of the DI into changed and unchanged classes. In the first step, coregistration plays a fundamental role and is a critical step. In practice, residual registration noises will sharply impact the performance of change detection. In this paper, we mainly focus on the second and the third steps. To be specific, we assume that the input multitemporal images have been coregistered, and then we can automatically perform DI generation and DI classification.

In the DI generation step, the log-ratio operator is the most widely used technique to obtain DI,¹⁵⁻¹⁷ since the log-ratio operator is concluded to be robust to calibration and radiometric errors. Thus, it can reduce the influence of speckle noise to some extent. However, we can still observe noisy regions in the DI generated by log-ratio operator. To solve the problem, Gao et al.¹⁷ proposed a modified log-ratio operator to restrain the negative effect of speckle noise. In the operator, the Gaussian distribution is used to model the DI to detect the concealed target in foliage. Zheng et al.¹⁸ proposed a DI generation framework that combines the edge information and local consistency of two kinds of classical operators (the subtraction operator and the log-ratio operator). The number of false alarms can be tuned in the combined DI. Hou et al.¹⁵ fused DIs generated by the Gauss-log ratio operator and the log-ratio operator by using discrete wavelet transform. In the fused image, the noise is suppressed and the performance of subsequent clustering is improved. As concluded by these methods, if the complementary information from multiple DI generation operators are properly fused, local consistency can be enhanced, and better DI representations can be obtained.

In the DI classification step of change detection, the pixels in DI are classified into changed class and unchanged class. The thresholding and clustering approaches are often used. In the thresholding methods, the expectation-maximization algorithm¹⁹ and generalized Kittler and Illingworth thresholding (K&I) algorithm²⁰ have been applied to select the optimal threshold. These approaches discriminate the changed and unchanged regions under the assumption that each class has a distinct mode in the histogram of DI. Thus, they often encounter difficulties when DI exhibits a unimodal histogram.²¹ To avoid the disadvantages of thresholding approaches, clustering algorithms are used to fit the patterns of changed and unchanged classes. Gong et al.²² proposed a reformulated fuzzy C-means (FCM) clustering algorithm for the classification of DI. Li et al.²³ designed a two-level clustering algorithm to discriminate the changed and unchanged pixels. The algorithm includes the first-level FCM clustering and the second-level nearest neighbor rule. These clustering methods are mainly implemented on DI and can suppress the effects of speckle noise to a certain degree. However, some information may get lost in the DI generation process. If representative features are directly extracted from two original images and a more accurate classification model is utilized, there is still considerable room to improve.

In this paper, a change detection method based on neighborhood-based ratio (NR) and extreme learning machine (ELM)²⁴ is proposed. NR operator is utilized for obtaining some pixels that have high probability of being changed or unchanged. Then, new image patches centered at these pixels are generated, and ELM is employed to train a model by using these patches. Finally, pixels in both original SAR images are classified by the pretrained ELM model. The ELM classification result and the preclassification result are combined to form the final change map. In this paper, we choose ELM as the classifier for SAR image change detection, since it is efficient and can provide good classification results.

There are two primary contributions in this research. First, inspired by Gong's work,²⁵ a preclassification scheme based on NR and hierarchical FCM clustering is designed to obtain some labeled samples of high accuracy for ELM. The second contribution is the adoption of ELM as the classification model for change detection.

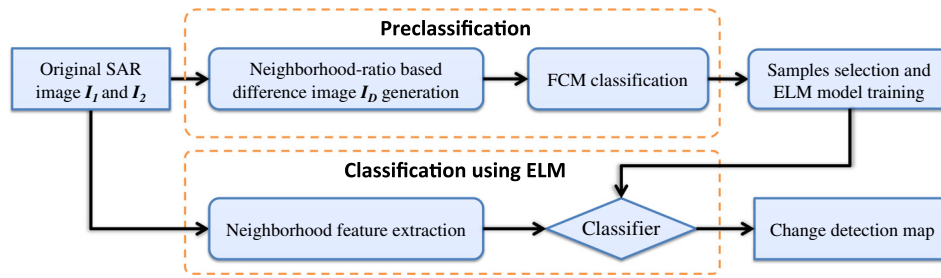


Fig. 1 Framework of the proposed change detection method.

The remainder of this paper is organized as follows. Section 2 is devoted to give problem statements and an overview of the proposed method. Section 3 provides a detailed description of the proposed change detection framework. Section 4 presents the experimental results with four SAR datasets. Finally, Sec. 5 makes several concluding remarks.

2 Problem Statements and Overview of the Proposed Method

Given two coregistered multitemporal SAR images, $I_1 = \{I_1(i, j), 1 \leq i \leq M, 1 \leq j \leq N\}$ and $I_2 = \{I_2(i, j), 1 \leq i \leq M, 1 \leq j \leq N\}$. Both images are polluted by speckle noise. The objective of change detection is to generate a change map, representing changes that occurred between the acquisition dates of two SAR images I_1 and I_2 . In other words, the change detection problem can be defined as a binary classification problem. A binary image associated with the changed and unchanged pixels is generated.

As shown in Fig. 1, the proposed change detection method is comprised of three main steps:

- Step 1. Preclassification based on NR and FCM: The NR operator is used to generate a DI. Then, the hierarchical FCM algorithm is utilized to select interested pixels that have high probability of being changed or unchanged. These interested pixels are selected as training samples for ELM, and the remaining pixels will be further classified in step 3.
- Step 2. Training a classifier by ELM: New image patches centered at interested pixels are generated directly from two original input SAR images. Pixelwise features are extracted directly from these patches. A classifier based on pixelwise patch features is trained by ELM.
- Step 3. Classification of changed and unchanged pixels: The remaining pixels in step 1 are further separated into changed and unchanged classes by using the pretrained classifier. Then, the classification result and the preclassification result in step 1 are combined to form the final change map.

3 Methodology

3.1 Preclassification by Using Neighborhood-Based Ratio and FCM

In order to generate good samples for ELM, pixels that have high probabilities of being changed or unchanged should be identified, and these pixels are selected as samples. In this paper, a scheme based on NR and hierarchical FCM clustering is designed to generate such pixels.

The NR operator is defined as

$$DI(m, n) = \theta \times \frac{\min\{I_1(m, n), I_2(m, n)\}}{\max\{I_1(m, n), I_2(m, n)\}} + (1 - \theta) \times \frac{\sum_{i \in \Omega \wedge i \neq m, n} \min\{I_1(m, n), I_2(m, n)\}}{\sum_{i \in \Omega \wedge i \neq m, n} \max\{I_1(m, n), I_2(m, n)\}}, \quad (1)$$

$$\theta = \frac{\sigma(m, n)}{\mu(m, n)}, \quad (2)$$

where $DI(m, n)$ is the gray level of a pixel on position (m, n) in the generated DI. It indicates the local similarity between I_1 and I_2 . $\sigma(m, n)$ denotes the variance of the gray level in neighborhood NR_{mn} . The size of NR_{mn} is $r \times r$. $\mu(m, n)$ denotes the mean of the gray level in the neighborhood NR_{mn} . The coefficient θ is a measure of the local heterogeneity: a low value of θ indicates that the local area is homogeneous, while a high value of θ indicates that the local area is heterogeneous. Therefore, if θ obtains a low value, the local area is homogeneous and the second part of (1) plays a leading role in DI generation. If θ obtains a high value, the local area is heterogeneous and the first part of (1) plays a leading role in DI generation.

After obtaining the DI by using the NR operator, we partition pixels in DI into three groups: the changed class Ω_c , unchanged class Ω_u , and intermediate class Ω_i . The pixels belonging to w_c and w_u have the high probability to be changed and unchanged. We observed that if we directly partition pixels into three classes by FCM, the intermediate class sometimes occupies a large part of the DI, therefore we can hardly obtain enough representative samples for ELM training. To address this issue, we use a hierarchical FCM clustering algorithm. The detailed description of the hierarchical FCM clustering algorithm is as follows:

- Input: The DI generated by NR operator.
- Step 1: Perform the FCM algorithm on DI to partition pixels into two clusters: Ω_c^1 and Ω_u^1 . The number of pixels in Ω_c^1 is denoted by T^1 . Then, the upper bound of the real changed class is defined as $TT = \sigma \cdot T^1$. Here, σ is set as 1.20 in our implementation.
- Step 2: Perform the FCM algorithm on DI to partition pixels into five clusters: $\Omega_1^2, \Omega_2^2, \dots, \Omega_5^2$. It should be noted that the five clusters are sorted by average values in descending order. Specifically, pixels in Ω_1^2 have the largest value, while pixels in Ω_5^2 have the smallest average value. Clusters with bigger average value denote that it is of higher probability to be a changed class. The number of pixels in the five clusters is defined as $T_1^2, T_2^2, \dots, T_5^2$, respectively. Set parameters $t = 1, c = T_1^2$. Assign the pixels in Ω_1^2 to the class Ω_c .
- Step 3: Set $t := t + 1, c := c + T_t^2$.
- Step 4: if $c < TT$, assign pixels in Ω_t^2 to the class Ω_i . Otherwise, assign pixels in Ω_t^2 to the class Ω_u . Go to step 3, and continue until $t = 5$.
- Output: As a result, the preclassification change map can be denoted as an image with labels $\{\Omega_c, \Omega_i, \Omega_u\}$.

After preclassification, we obtain a change map with labels $\Omega_c, \Omega_i, \Omega_u$. The pixels belonging to Ω_c have the high probability to be changed, while the pixels belonging to Ω_u have the high probability to be unchanged. These two kinds of pixels can be chosen as samples. The classification of pixels belonging to Ω_i will be described in the following section.

3.2 Classification by Using Extreme Learning Machine

For SAR image change detection, the analysis of the nonlinear relations from multitemporal SAR images is very important. In this paper, ELM is utilized as the classifier, since it can be easily adapted to different conditions, and is capable of capturing the nonlinear relations of multitemporal SAR images. In this section, we first briefly review the ELM classifier, and then provide a detailed description of the proposed classification framework.

3.2.1 Extreme learning machine

ELM²⁴ is a neural network with only one hidden layer and one linear output layer. The structure of ELM is shown in Fig. 2. The training samples are represented as $\{x_j, y_j\}_{j=1}^{N_s}$, where $x \in \mathbb{R}^d$ and $y \in \mathbb{R}$, N_s is the number of samples. Given input samples, the output of ELM having L hidden nodes is modeled by

$$\sum_{i=1}^L \beta_i f(w_i x_j + b_i) = y_j, \quad j = 1, \dots, N_s, \quad (3)$$

where β_i denotes the weight vector connecting the i 'th hidden node to the output nodes, $f(\cdot)$ is a nonlinear activation function, w_i denotes the weight vector connecting the i 'th hidden node to

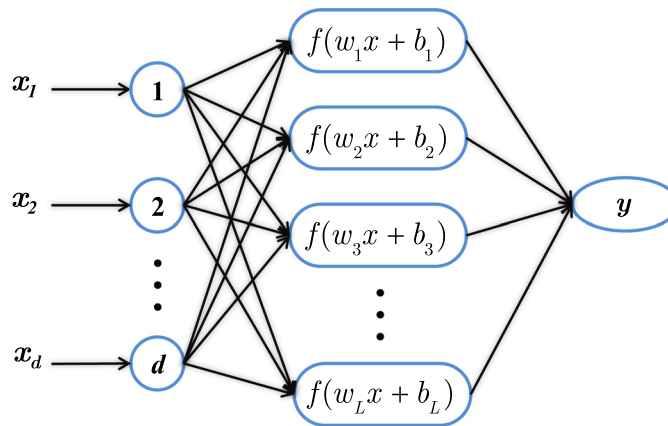


Fig. 2 Structure of ELM.

the input nodes, and b_i is the bias of the i 'th hidden node. Equation (3) can be rewritten in a compact form as

$$\mathbf{H}\beta = \mathbf{Y}, \tag{4}$$

where $\mathbf{Y} = [y_1, y_2, \dots, y_{N_s}]^T$, $\beta = [\beta_1, \beta_2, \dots, \beta_L]^T$ is a vector consisting of the output weights between the hidden layer of L nodes and the output node. \mathbf{H} denotes the hidden layer output matrix and is defined as

$$\mathbf{H} = \begin{bmatrix} f(w_1x_1 + b_1) & \cdots & f(w_Lx_1 + b_L) \\ \vdots & \cdots & \vdots \\ f(w_1x_N + b_1) & \cdots & f(w_Lx_N + b_L) \end{bmatrix}_{N_s \times L}. \tag{5}$$

The j 'th row of \mathbf{H} is the output vector of the hidden layer corresponding to the input x_j . The i 'th column of \mathbf{H} is the output of the i 'th hidden node corresponding to the inputs x_1, x_2, \dots, x_{N_s} . Optimal weights and bias can be found by using backpropagation learning algorithms. However, there is no guarantee that the global minimum error can be found.²⁶ Therefore, local minima and overtraining may occur in the learning process. Researchers found that, in most cases, the number of hidden nodes is much smaller than the number of training samples ($L \ll N_s$); the smallest norm least-squares of Eq. (4) can be denoted as

$$\beta' = \mathbf{H}^\dagger \mathbf{Y}, \tag{6}$$

where \mathbf{H}^\dagger is the Moore–Penrose generalized inverse of matrix \mathbf{H} . Thus, Eq. (6) gets the smallest norm of weights with the best generalization performance. In addition, it involves no local minima.

The training process of the ELM algorithm can be conducted as the following three steps: (1) randomly assign values to hidden node parameters. Specifically, randomly choose input weight $\{w_1, w_2, \dots, w_{N_s}\}$, and randomly assign values to bias $\{b_1, b_2, \dots, b_{N_s}\}$. (2) Compute the hidden layer output matrix \mathbf{H} . (3) Calculate the output weight $\beta = \mathbf{H}^\dagger \mathbf{Y}$.

3.2.2 Classification of changed and unchanged pixels

The process of changed and unchanged pixels classification is comprised of three steps. First, neighborhood features of sample pixels (belonging to Ω_c and Ω_u) are generated. Second, an ELM classifier is trained based on these features. Next, the neighborhood features of pixels belonging to Ω_i are fed into the pretrained ELM classifier, and these pixels are classified into the changed and unchanged classes.

The process of neighborhood features generation is shown in Fig. 3. First, image patches of interested positions (pixels belonging to Ω_c and Ω_u obtained in Sec. 3.1) are generated. These

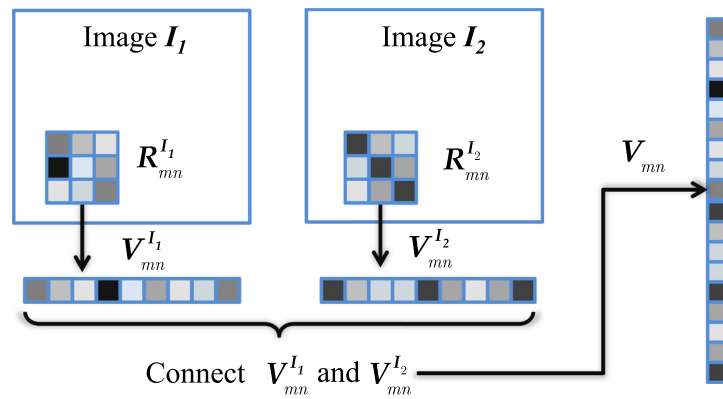


Fig. 3 Neighborhood features generation for each interested position as ELM inputs.

image patches contain enough change information around the positions. As shown in Fig. 2, let $R_{mn}^{I_1}$ represent a patch with the center at position (m, n) in image I_1 and the size of $R_{mn}^{I_1}$ is $k \times k$. $R_{mn}^{I_2}$ represents the corresponding patch in image I_2 . Convert $R_{mn}^{I_1}$ and $R_{mn}^{I_2}$ to vectors $V_{mn}^{I_1}$ and $V_{mn}^{I_2}$, respectively. Both vectors are concatenated and form a new vector V_{mn} as shown in Fig. 3. V_{mn} denotes the sample feature vector at the position (m, n) .

The extracted neighborhood features are then fed into ELM to train a classifier. By using the trained ELM classifier, pixels belonging to Ω_i are further separated into changed and unchanged classes. Finally, we combine the ELM classification result and the preclassification result together to form the final change map.

4 Experimental Results and Analysis

4.1 Dataset Description and Experimental Settings

In order to evaluate the effectiveness of the proposed method, we apply the proposed method to three real SAR datasets with different characteristics. In addition, to demonstrate that the proposed method is effective in low signal–noise ratio (SNR) scenarios, we use one simulated dataset to test the performance of the proposed method.

Results of four other state-of-the-art techniques for change detection are given for comparison purpose. These methods are PCAKM,²⁷ NR,²⁵ MRFFCM,²⁸ and GaborTLC.²³ Results of PCAKM, MRFFCM, and GaborTLC are implemented by using the authors' publicly available code. Therefore, these methods are implemented using the default parameters provided in their source code. Specifically, in PCAKM, $h = 5$ and $S = 3$ are used. In MRFFCM, the number of subintervals is set to 30 as mentioned in Ref. 28. In GaborTLC, $f = \sqrt{2}$, $U = 8$, $V = 5$, and $k_{\max} = 2\pi$ are used. Since we cannot find the source code of NR, we implemented NR in MATLAB[®]. The neighborhood size in NR is set to 3 as mentioned in Ref. 25. The MATLAB[®] implementation of the proposed method is available at Ref. 29. We first introduce the dataset, and then give a brief introduction to some evaluation criteria of the experimental results.

The first dataset used in the experiment is the Bern dataset. It consists of two SAR images acquired by ERS-2 Satellite. The images were captured in April and May 1999, respectively. Between the two dates, the River Aare flooded entirely parts of Bern. The available ground truth that is shown in Fig. 4(c) was created by integrating prior information with photo interpretation.

The second dataset, as shown in Fig. 5, is called the Ottawa dataset. It represents a section (290×350 pixels) of two SAR images over the city of Ottawa acquired by RADARSEAT SAR sensor. The dataset was provided by the Defense Research and Development Canada, Ottawa. It contains two images acquired in May and August 1997, respectively. The images present changed areas where they were once afflicted with floods. The ground truth, shown in Fig. 5(c), was created by integrating prior information with photo interpretation.

The third dataset, as shown in Fig. 6, is called the San Francisco dataset. It presents a section (256×256 pixels) of two SAR images acquired by the ERS-2 SAR sensor. The original images

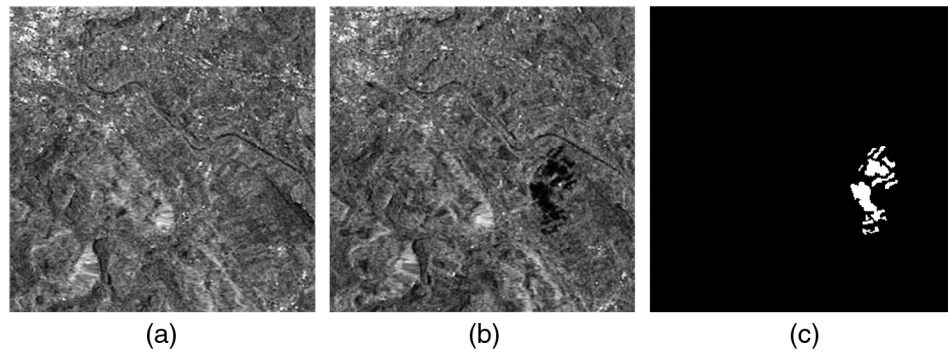


Fig. 4 Inland water dataset. (a) Image acquired in June 2008. (b) Image acquired in June 2009. (c) Ground-truth image.

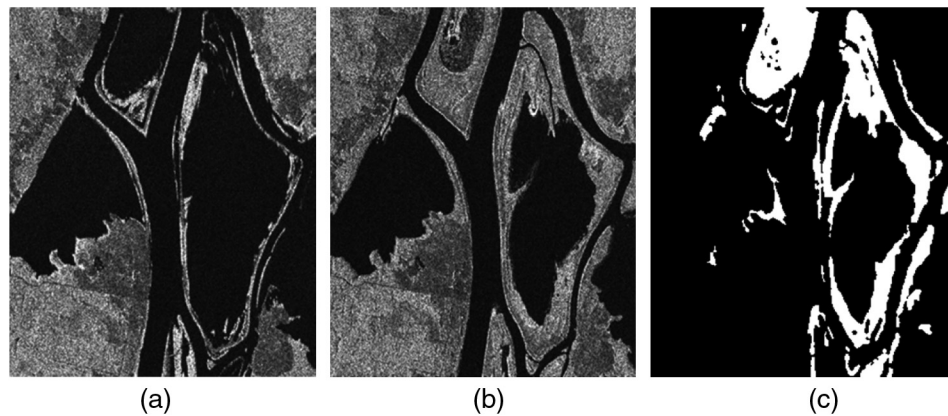


Fig. 5 Ottawa dataset. (a) Image acquired in May 1997. (b) Image acquired in August 1997. (c) Ground-truth image.

are 7749×7713 pixels and are available in Ref. 30. The images were captured in August 2003 and May 2004, respectively. The ground truth change map shown in Fig. 6(c) is generated by integrating prior information with photo interpretation based on the input images in Figs. 6(a) and 6(b).

The fourth dataset, as shown in Fig. 7, is one simulated dataset. The size of the dataset is 350×250 pixels. The effect of speckle noise on the dataset is quite large. The ground truth image is given in Fig. 7(c).

The performance evaluation of SAR image change detection is an important issue. In this paper, the quantitative analysis of the change detection results is set as follows: false positives

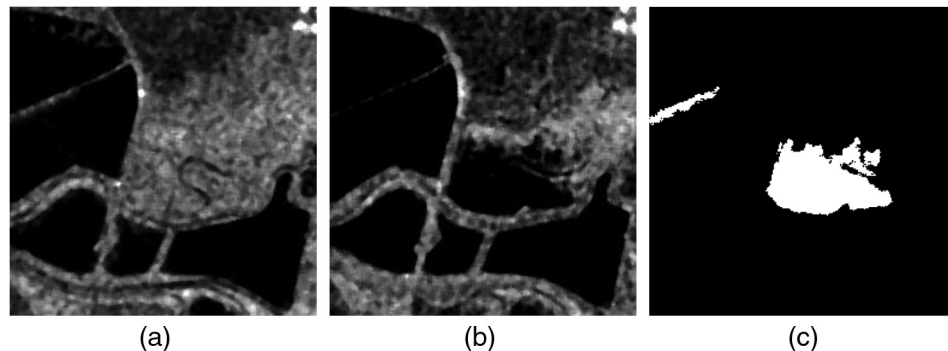


Fig. 6 San Francisco dataset. (a) Image acquired in August 2003. (b) Image acquired in May 2004. (c) Ground-truth image.

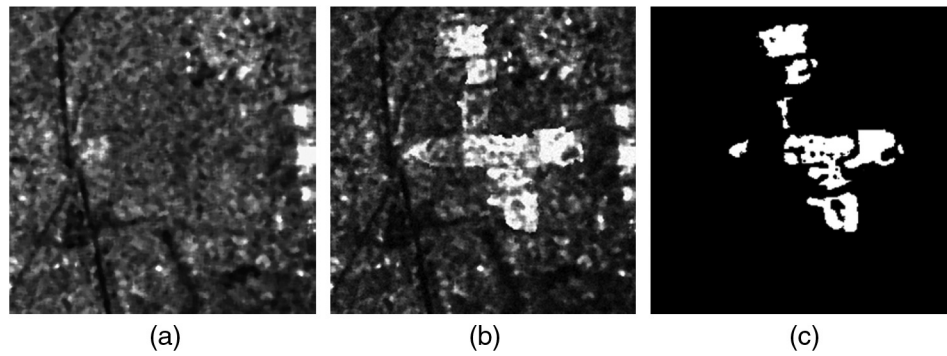


Fig. 7 Simulated dataset. (a) Image changed before. (b) Image changed after. (c) Ground-truth image.

(FP), false negatives (FN), overall errors (OE), percentage correct classification (PCC), and Kappa coefficient (KC). In the binary ground truth image, we count the actual number of pixels belonging to the unchanged class and the changed class (denoted by N_u and N_c , respectively). On the other hand, we compare the binary ground truth image with the one generated by a certain method pixel by pixel. Then, FPs denote the number of pixels belonging to the unchanged class but that are falsely classified as changed class. FNs are the number of pixels belonging to the changed class but that are falsely classified as unchanged class. The OEs are the sum of FP and FN. PCC is given by $PCC = (N_u + N_c - FP - FN) / (N_u + N_c) \times 100\%$. KC gives the percentage of agreement (correct classified pixels) corrected by the number of agreements that would be expected purely by chance. Specifically, KC is defined as

$$KC = \frac{PCC - PRE}{1 - PRE}, \quad (7)$$

where

$$PRE = \frac{(N_c - FN + FP) \cdot N_c + (N_u - FP + FN) \cdot N_u}{(N_c + N_u) \cdot (N_c + N_u)}. \quad (8)$$

It is well worth noting that KC relies on the dependent values of FP and FN, while PCC relies only on the sum value of FP and FN. Therefore, KC is a more persuasive coefficient than PCC because more detailed information is involved.²⁸

4.2 Test of the Parameter r

The first experiment is a test of parameter r , which means the size of neighborhood in the NR operator. It is selected as the test parameter because it is related to the accuracy of preclassification. In this experiment, r ranges from 3 to 11 and is of some discrete values. The three real SAR datasets are experimented on, and the deliberate criterion KC is employed here. The results are shown in Fig. 8. The three curves show that the values of KC decrease obviously along with the enlargement of r . Therefore, in our following experiments, we set the neighborhood size of the NR operator as 3×3 .

4.3 Test of the Parameter k

The second experiment is a test of parameter k , which stands for the neighborhood size in feature extraction. The size of the neighborhood is an important parameter that can affect the final change detection results. The three real SAR datasets are experimented on, and the PCC is employed as the criterion here. As shown in Fig. 9, we set k to 3, 5, 7, 9, 11, and 13 to indicate the relationship between k and PCC . The ELM classifier requires a neighborhood patch big enough for feature learning; if k is set as 3, the result is sensitive to neighborhood noise. Furthermore, when $k \geq 7$, the result tends to get worse, since the neighborhood features are

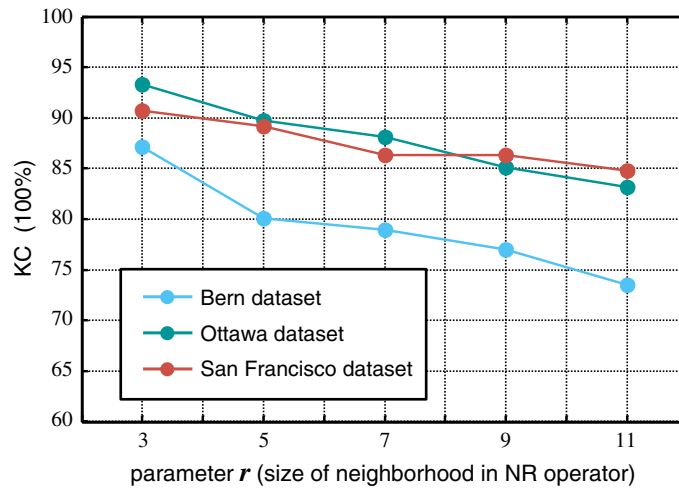


Fig. 8 Relationship between KC and the neighborhood of NR operator on three real SAR datasets.

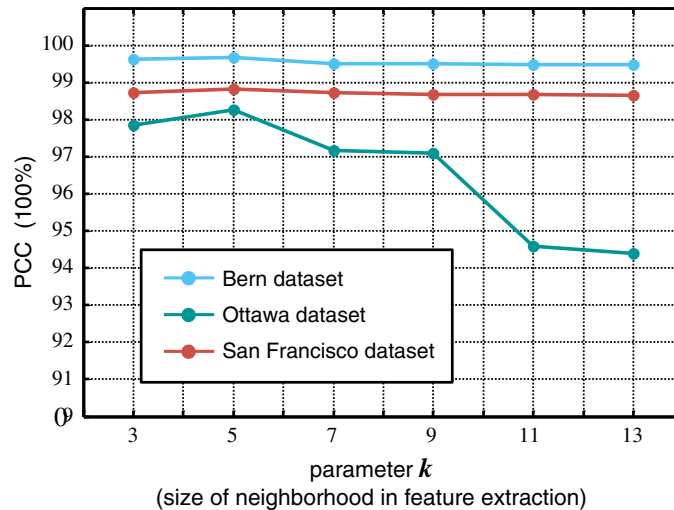


Fig. 9 Relationship between PCC and the parameter k on three real SAR datasets.

not representative for the specified position. When k is set to 5, the proposed method achieves the best performance on three datasets. Hence, setting $k = 5$ is the best choice for feature extraction. In our following experiments, we use a neighborhood of 5 pixels for feature extraction with ELM.

4.4 Results on the Bern Dataset

The results of the experiments on the three datasets are exhibited in two ways: the final change maps in figure form and the criteria in tabular form. Figure 10 shows the final change maps of various methods on the Bern dataset, and Table 1 lists the values for evaluation. In the table, the results of the proposed method are written in bold.

Table 1 shows that for the MRFFCM, some unchanged pixels are falsely classified into changed class (appearing as a high value of FP). In Figs. 10(a) and 10(b), some noise spots are falsely detected by PCAKM and NR. However, fewer noise points are generated by the proposed method compared with the other methods. FN and FP of the proposed method do not exhibit the best, whereas PCC and KC are the best. It should be noted that the value

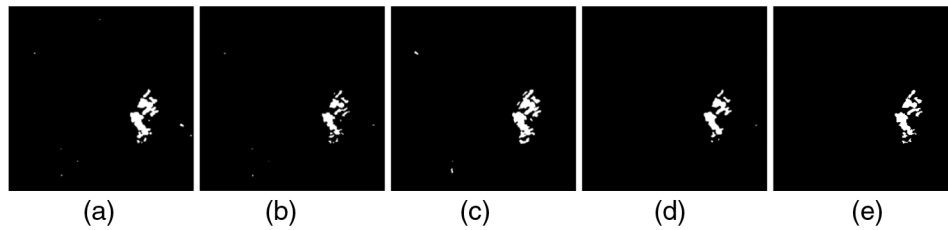


Fig. 10 Visualized results of various change detection methods on the Bern dataset. (a) Result by PCAKM.²⁷ (b) Result by NR.²⁵ (c) Result by MRFFCM.²⁸ (d) Result by GaborTLC.²³ (e) Result by the proposed method.

Table 1 Change detection results of different methods on the Bern dataset.

Methods	FP	FN	OE	PCC (%)	KC (%)
PCAKM ²⁷	247	119	366	99.60	84.78
NR ²⁵	110	199	309	99.66	85.91
MRFFCM ²⁸	364	47	411	99.55	84.13
GaborTLC ²³	135	173	308	99.66	86.27
Proposed method	147	146	293	99.68	87.16

of KC is the most cogent and discriminative criterion. The results indicate that the proposed method outperforms the other methods and is capable of improving the change detection accuracy.

4.5 Results on the Ottawa Dataset

As for the Ottawa dataset, the results are shown in Fig. 11 and listed in Table 2. As shown in Fig. 11(b), the change map generated by NR is polluted by many white noise spots. It is due to the fact that the NR is sensitive to the saltation of gray level. As pointed out by red arrows in Figs. 11(a) and 11(d), some changed regions are missing compared with the change map generated by the proposed method. Therefore, the value of FN of PCAKM and GaborTLC appears higher than the proposed method. As shown in Fig. 11(c), the MRFFCM classifies some small unchanged pixels into changed class and it yields a high FP. By contrast, the proposed method achieves the best change detection result after feature extraction and ELM classification, as shown in Fig. 11(e).

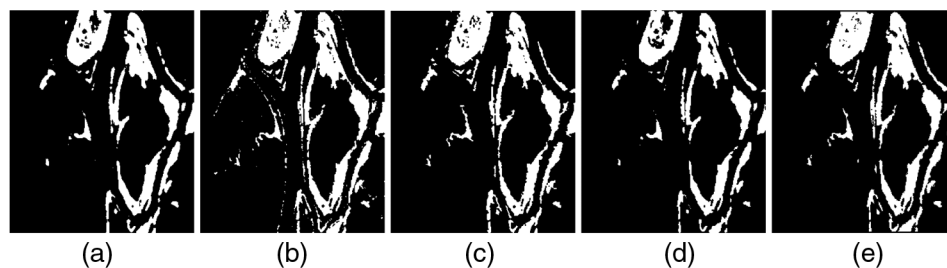
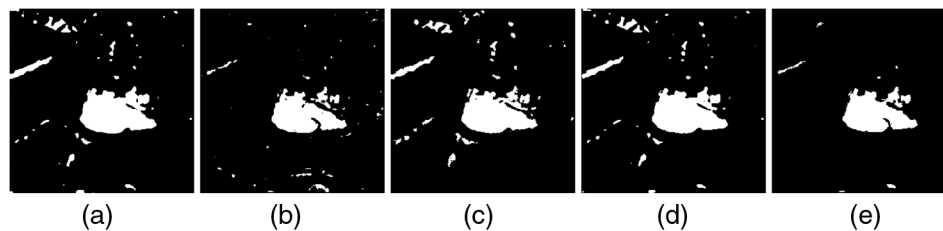


Fig. 11 Visualized results of various change detection methods on the Ottawa dataset. (a) Result by PCAKM.²⁷ (b) Result by NR.²⁵ (c) Result by MRFFCM.²⁸ (d) Result by GaborTLC.²³ (e) Result by the proposed method.

Table 2 Change detection results of different methods on the Ottawa dataset.

Methods	FP	FN	OE	PCC (%)	KC (%)
PCAKM ²⁷	960	1515	2475	97.56	90.43
NR ²⁵	1914	727	2641	97.40	90.25
MRFFCM ²⁸	1636	712	2348	97.69	91.27
GaborTLC ²³	253	2531	2784	97.26	88.71
Proposed method	954	812	1766	98.26	93.30

**Fig. 12** Visualized results of various change detection methods on the San Francisco dataset. (a) Result by PCAKM.²⁷ (b) Result by NR.²⁵ (c) Result by MRFFCM.²⁸ (d) Result by GaborTLC.²³ (e) Result by the proposed method.**Table 3** Change detection results of different methods on the San Francisco dataset.

Methods	FP	FN	OE	PCC (%)	KC (%)
PCAKM ²⁷	1618	25	1643	97.49	83.68
NR ²⁵	556	741	1297	98.02	84.82
MRFFCM ²⁸	1511	191	1702	97.40	82.69
GaborTLC ²³	1376	60	1436	97.81	85.39
Proposed method	182	596	778	98.81	90.68

4.6 Results on the San Francisco Dataset

The change detection results generated by the different methods on the San Francisco dataset are shown in Fig. 12 and listed in Table 3. There are many white spots in the change map generated by the PCAKM, MRFFCM, and GaborTLC, which are listed as high values of FP in Table 3. These white spots are eliminated to some extent by the proposed method, since the proposed method can learn meaningful features from neighborhood pixels. From Table 3, we can see that the proposed method obtains the smallest OE value and the maximum KC value. No matter whether the change areas are small (Bern and San Francisco dataset) or large (Ottawa dataset), the proposed method can find a balance between denoising and preserving details.

4.7 Results on Simulated Datasets

As mentioned before, we use one simulated dataset to test the performance of different change detection methods. The effect of speckle noise on the dataset is quite large. The change detection results generated by the proposed method compared together with closely related methods on the simulated dataset are shown in Fig. 13 and listed in Table 4. There are many noise regions in the change map generated by the PCAKM, NR, MRFFCM, and GaborTLC. Therefore, the FP

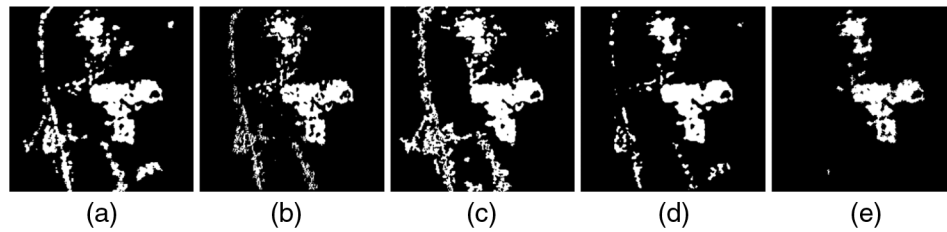


Fig. 13 Visualized results of various change detection methods on the simulated dataset. (a) Result by PCAKM.²⁷ (b) Result by NR.²⁵ (c) Result by MRFFCM.²⁸ (d) Result by GaborTLC.²³ (e) Result by the proposed method.

Table 4 Change detection results of different methods on the simulated dataset.

Methods	FP	FN	OE	PCC (%)	KC (%)
PCAKM ²⁷	5588	544	6132	90.94	50.81
NR ²⁵	3567	871	4438	93.23	57.44
MRFFCM ²⁸	6883	232	7115	89.14	48.67
GaborTLC ²³	2866	570	3436	94.76	65.91
Proposed method	1090	897	1987	96.97	87.40

values of these methods are listed as high values in Table 4. By contrast, the proposed method achieves the best change detection result, as shown in Fig. 13(e). The experimental results on the simulated dataset demonstrate that the proposed method is effective in low SNR scenarios.

5 Conclusions

In this paper, we presented an SAR image change detection method based on NR and ELM. Existing SAR image change detection methods usually generate a DI first, and use clustering methods to classify the pixels of DI into changed class and unchanged class. Some useful information may get lost in the DI generation process. The proposed method uses ELM exploits representative neighborhood features directly from multitemporal SAR images. Compared with four closely related methods, the proposed method exhibits good performance. In the future, we will do research on detecting changed point targets. In addition, we will continue to investigate the proposed method to detect the development of urban zones or the movement of glaciers over time.

Acknowledgments

The authors would like to thank all the anonymous reviewers for their very competent comments and helpful suggestions. This work was supported by the National Natural Science Foundation of China (Grant Nos. 41606198, 61271405, 61576011, and 61401413) and in part by the China Postdoctoral Science Foundation under Grant No. 2015M582140.

References

1. L. Jia et al., "SAR image change detection based on iterative label-information composite kernel supervised by anisotropic texture," *IEEE Trans. Geosci. Remote Sens.* **53**(7), 3960–3973 (2015).
2. D. Huong and R. Nagasawa, "Potential flood hazard assessment by integration of ALOS PALSAR and ASTER GDEM: a case study for the Hoa Chau commune, Hoa Vang district, in central Vietnam," *J. Appl. Remote Sens.* **8**(1), 083626 (2014).

3. J. Shang et al., "Estimating plant area index for monitoring crop growth dynamics using Landsat-8 and RapidEye images," *J. Appl. Remote Sens.* **8**(1), 085196 (2014).
4. Y. Yang et al., "Using multitemporal Landsat imagery to monitor and model the influences of landscape pattern on urban expansion in a metropolitan region," *J. Appl. Remote Sens.* **8**(1), 083639 (2014).
5. Z. Sun et al., "Long-term effects of land use/land cover change on surface runoff in urban areas of Beijing, China," *J. Appl. Remote Sens.* **8**(1), 084596 (2013).
6. S. Pettinato et al., "Snow cover area identification by using a change detection method applied to COSMO-SkyMed images," *J. Appl. Remote Sens.* **8**(1), 084684 (2014).
7. C. Berger et al., "Multi-modal and multi-temporal data fusion: outcome of the 2012 GRSS data fusion contest," *IEEE J. Sel. Top. Appl. Earth Obs. Remote Sens.* **6**(3), 1324–1340 (2013).
8. C. Zhong, Q. Xu, and B. Li, "Relative radiometric normalization for multitemporal remote sensing images by hierarchical regression," *IEEE Geosci. Remote Sens. Lett.* **13**(2), 217–221 (2016).
9. T. Ahmed, D. Singh, and B. Raman, "Potential application of Kanade-Lucas-Tomasi tracker on satellite images for automatic change detection," *J. Appl. Remote Sens.* **10**(1), 026018 (2016).
10. X. Zhang, C. Glennie, and A. Kusari, "Change detection from differential airborne LiDAR using a weighted anisotropic iterative closest point algorithm," *IEEE J. Sel. Top. Appl. Earth Obs. Remote Sens.* **8**(7), 3338–3346 (2015).
11. J. Yang and W. Sun, "Automatic analysis of the slight change image for unsupervised change detection," *J. Appl. Remote Sens.* **9**(1), 095995 (2015).
12. H. Aghababae, Y.-C. Tzeng, and J. Amini, "Swarm intelligence and fractals in dual-pol synthetic aperture radar image change detection," *J. Appl. Remote Sens.* **6**(1), 063596 (2012).
13. H. Hu and Y. Ban, "Unsupervised change detection in multitemporal SAR images over large urban areas," *IEEE J. Sel. Top. Appl. Earth Obs. Remote Sens.* **7**(8), 3248–3261 (2014).
14. T. Celik, "Change detection in satellite images using a generic algorithm approach," *IEEE Geosci. Remote Sens. Lett.* **7**(2), 386–390 (2010).
15. B. Hou et al., "Unsupervised change detection in SAR image based on gauss-log ratio image fusion and compressed projection," *IEEE J. Sel. Top. Appl. Earth Obs. Remote Sens.* **7**(8), 3297–3317 (2014).
16. Y. Bazi, L. Bruzzone, and F. Melgani, "An unsupervised approach based on the generalized Gaussian model to automatic change detection in multi-temporal SAR images," *IEEE Trans. Geosci. Remote Sens.* **43**(4), 874–887 (2005).
17. G. Gao et al., "Modified log-ratio operator for change detection of synthetic aperture radar targets in forest concealment," *J. Appl. Remote Sens.* **8**(1), 083583 (2014).
18. Y. Zheng et al., "Using combined difference image and k-means clustering for SAR image change detection," *IEEE Geosci. Remote Sens. Lett.* **11**(3), 691–695 (2014).
19. L. Bruzzone and D. F. Prieto, "Automatic analysis of the difference image for unsupervised change detection," *IEEE Trans. Geosci. Remote Sens.* **38**(3), 1171–1182 (2000).
20. G. Moser and S. B. Serpico, "Generalized minimum-error thresholding for unsupervised change detection from SAR amplitude imagery," *IEEE Trans. Geosci. Remote Sens.* **44**(10), 2972–2982 (2006).
21. F. Bovolo and L. Bruzzone, "A split-based approach to unsupervised change detection in large-size multitemporal images: application to tsunami-damage assessment," *IEEE Trans. Geosci. Remote Sens.* **45**(6), 1658–1670 (2007).
22. M. Gong, Z. Zhou, and J. Ma, "Change detection in synthetic aperture radar images based on image fusion and fuzzy clustering," *IEEE Trans. Image Process.* **21**(4), 2141–2151 (2012).
23. H. C. Li et al., "Gabor feature based unsupervised change detection of multitemporal SAR images based on two-level clustering," *IEEE Geosci. Remote Sens. Lett.* **12**(12), 2458–2462 (2015).
24. G. Huang et al., "Extreme learning machine for regression and multiclass classification," *IEEE Trans. Syst., Man, Cybern. B* **42**(2), 513–529 (2012).

25. M. Gong, Y. Cao, and Q. Wu, "A neighborhood-based ratio approach for change detection in SAR images," *IEEE Geosci. Remote Sens. Lett.* **9**(2), 307–311 (2012).
26. A. Samat et al., "E2LMs: ensemble extreme learning machines for hyperspectral image classification," *IEEE J. Sel. Top. Appl. Earth Obs. Remote Sens.* **7**(4), 1060–1069 (2014).
27. T. Celik, "Unsupervised change detection in satellite images using principal component analysis and k-means clustering," *IEEE Geosci. Remote Sens. Lett.* **6**(4), 772–776 (2009).
28. M. Gong et al., "Fuzzy clustering with a modified MRF energy function for change detection in synthetic aperture radar images," *IEEE Trans. Fuzzy Syst.* **22**(1), 98–109 (2014).
29. Feng Gao's Homepage, <http://fenggao.sinaapp.com>.
30. Earthnet Online, http://earth.esa.int/ers/ers_action/SanFrancisco_SAR_IM_Orbit_47426_20040516.html (22 November 2016).

Feng Gao is currently a lecturer at the College of Information Science and Engineering, Ocean University of China. He acquired his BS degree in software engineering from Chongqing University, China, in 2008, and received his PhD in computer science from Beihang University, China, in 2015. His research interests include information fusion, computer vision, and image understanding.

Junyu Dong received his BS and MS degrees in applied mathematics from Ocean University of China in 1993 and 1999, respectively. He received his PhD in image processing in 2003 from the School of Mathematical and Computer Sciences, Heriot-Watt University, UK. He is currently a professor of computer science and head of the Computer Science and Technology Department in Ocean University of China.

Bo Li received his BS degree from Chongqing University, China, in 1986, his MS degree from Xi'an Jiaotong University, China, in 1989, and his PhD from Beihang University, China, in 1993, all in computer science. Currently, he is a professor of computer science and engineering and the director of the Beijing Key Laboratory of Digital Media in Beihang University.

Qizhi Xu is currently an associate professor of computer science and engineering in Beihang University. He received his BS degree in computer science from Jiangxi Normal University, Jiangxi, China, in 2005, and his PhD in computer science from Beihang University, Beijing, China, in 2012. His research interests include image registration, information fusion, computer vision, and image understanding.

Cui Xie is currently a lecturer at the College of Information Science and Engineering, Ocean University of China. She acquired her PhD in Key Laboratory of Marine Simulation and Control for Ministry of Communications, Dalian Maritime University, China, in 2005. Her research interests include computer graphics, visualization, and computer vision.